International Journal of Fracture **114:** 379–399, 2002.

Studies on bridging tractions – simultaneous bridging tractions and COD measurements

M. STUDER[1], J. PIETRZYK[1], K. PETERS[2], J. BOTSIS[1,*] and P. GIACCARI[3]
[1]*Laboratory of Applied Mechanics and Reliability Analysis, Department of Mechanical Engineering, Ecole Polytechnique Fédérale de Lausanne, CH 1015 Lausanne, Switzerland*
[2]*Department of Mechanical and Aerospace Engineering, North Carolina State University, Box 7910, Raleigh, NC 27695, U.S.A.*
[3]*Institute of Applied Optics, Department of Microengineering, Ecole Polytechnique Fédérale de Lausanne, CH 1015 Lausanne, Switzerland*
*(*Author for correspondence: (E-mail address: john.botsis@epfl.ch)*

Received 12 April 2001; accepted in revised form 29 January 2002

Abstract. The main objective of this work is to investigate the bridging tractions in a model composite using optical fiber Bragg grating (FBG) sensors written into selected reinforcing fibers. Simultaneously, the crack opening displacement (COD) is measured using a speckle interferometry technique. The measurements are useful in the verification of the relation between the COD and bridging tractions established with the use of the weight function method. Center crack specimens made of epoxy and reinforced with one layer of optical fibers are prepared and tested under remote tension parallel to the fibers. Bragg gratings of 0.17 to 0.38 mm in length are introduced in selected fibers for direct, non invasive, local measurements of axial strains in these fibers. A controlled central crack, bridged by intact fibers, is introduced by a laser technique such that the FBGs are located between the crack faces. The results on the forces obtained from the FBGs and the COD-weight function method show good agreement. The experimental results also compare very well with 3-dimensional numerical simulations of the actual specimen geometry and loading configuration.

1. Introduction

As compared to their homogeneous counterparts, composite materials offer increased resistance to fracture due to several sources for energy absorption during fracture. In long fiber reinforced composites, crack bridging by intact fibers is considered one of the most efficient mechanisms in reducing the stress level at the vicinity of a transverse crack. Moreover, the bridging phenomenon can absorb energy through fiber-matrix debonding and frictional sliding. Thus, a quantitative characterization of the bridging phenomenon is essential in order to model fracture in composite materials. This includes a direct measurement of the bridging tractions, crack opening displacement (COD) and debonding for a given composite material.

Several analytical models have been presented in the literature to describe fiber crack bridging (Aveston et al., 1971; Budiansky et al., 1986; Marshall et al., 1985; McCartney, 1987; Thouless, 1989; Yang et al., 1991; Budiansky and Amazigo, 1989; Rubinstein and Xu, 1992; Nemat-Nasser and Hori, 1987; Buchanan et al., 1997; Cox and Marshall, 1991; Chen and Chang, 1997). Most of them are based on the assumption that the action of the bridging fibers can be well approximated by a closing pressure acting on the crack faces. In some models the closing pressure is derived using shear lag analysis, while in others a constant closing pressure is assumed. Other works relate the closing tractions to the crack opening displacement (COD).

Thus, when experimental data on COD are available, the COD-bridging traction relation offers an indirect method to measure the tractions. Such methods, already proved useful, necessitate highly accurate measurements of the COD profiles for reliable evaluations of the associated bridging tractions.

Recently, a direct measure of bridging forces in a sapphire-epoxy composite using fluorescence spectroscopy was performed by Belnap and Shetty (1998). This powerful technique allows one to measure the axial strain in the embedded fiber, yet it requires a transparent matrix. Similarly, optical fiber Bragg grating (FBG) sensors permit the measurement of the strain along the optical fiber axis over the entire length of the Bragg grating and have been used in a number of applications (Measures, 1992; Carman and Sendeckyj, 1995). Their small size, precision, insensitivity to electrical fields, ease of embedment, and extremely short length (e.g., 0.17 mm) make the FBG strain gauge an ideal tool to determine tractions in the bridging zone. Further, if the Bragg grating is fabricated sufficiently long the method can provide information on the stress distribution along the fiber axis (Peters et al., 2001). The latter, being of decisive importance for the characterization of the interaction between the fiber and the matrix, may allow one to determine the regions in the fiber-matrix interface where debonding and friction occur.

The use of the FBG sensors to determine the bridging tractions combined with the simultaneous measurement of the COD profiles by electronic speckle pattern interferometry (ESPI) can be very useful in the verification of the relation between the COD and the bridging tractions established with the use of the weight function method (Cox and Marshall, 1991; Beuckner, 1970) or other analytical method. Therefore, the main objective of this work is to investigate the bridging tractions in a model composite material using FBG sensors written into the reinforcing fibers in the central cracked (CC) specimen simultaneous to COD measurements. The matrix material is an epoxy and the reinforcement consists of one layer of optical fibers. A Bragg grating is introduced in selected fibers for a direct non-invasive measurement of the strains over the length of the grating. The experimental results are compared with calculations using experimental COD data and a 2-dimensional (2D) weight function method, as well as 3-dimensional (3D) numerical simulations of the actual specimen-load configuration. The paper is organized as follows: in Section 2 the weight function method and its implementation in this work is outlined. Also given in this section are the main points of the 3D Finite Element model (FEM) and the strain response of the FBG sensors. The experimental methods are described in Section 3. Results and discussion on the bridging tractions are given in Section 4 and conclusions in Section 5. Details of the numerical implementation of the weight function method are given in Appendix A.

2. Background

2.1. Bridging tractions – crack opening relations

Cox and Marshall (1991) outlined a 2D formulation to calculate the COD as a function of the remote load, σ_∞, and bridging tractions, $\varphi(x)$, acting along the crack surfaces. The relevant parameters of this formulation are shown in Figure 1. In this work, an approach to determine the bridging tractions from experimental COD data, suggested in Cox and Marshall (1991) is developed into a form appropriate for discrete reinforcing fibers.

The bridging tractions are assumed to act symmetrically on the two crack faces. Thus, the COD is given by

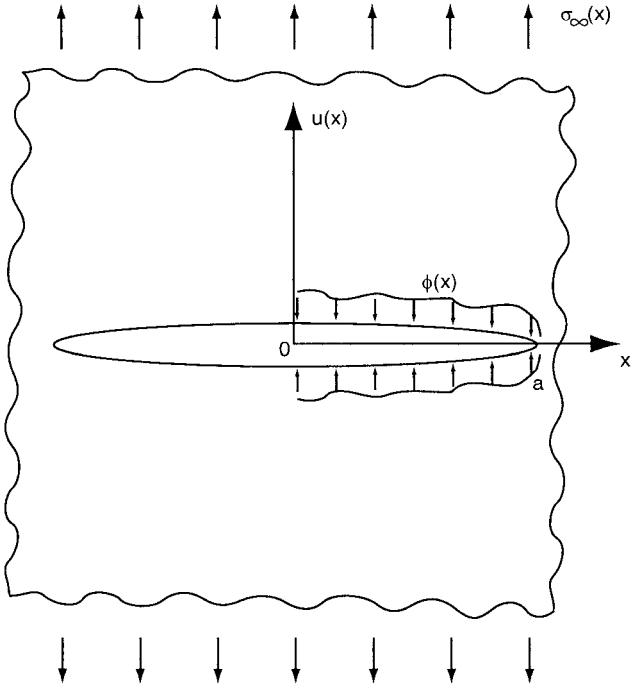

Figure 1. Crack geometry showing COD, $u(x)$, remote stress, $\sigma_\infty(x)$, bridging tractions, $\phi(x)$, and crack length, a.

$$u(x) = u_\infty(x) - \frac{4}{E'}\left\{\int_x^a \left[\int_0^{a'} g(x', a', w)\varphi(x')\,\mathrm{d}x'\right] g(x, a', w)\,\mathrm{d}a'\right\}, \tag{1}$$

where $u_\infty(x)$ is the COD due to the remote load given by

$$u_\infty(x) = \frac{4}{E'}\left\{\int_x^a \left[\int_0^{a'} g(x', a', w)\sigma_\infty(x')\,\mathrm{d}x'\right] g(x, a', w)\,\mathrm{d}a'\right\}.$$

The function $g(x, a, w)$ is a known influence function of the specimen geometry. Assuming a homogeneous material, the parameter E' is a function of the elastic constants depending upon the type of anisotropy and state of stress (Tada et al., 2000). In this work we used the function corresponding to an orthotropic plate under plane stress and the elastic constants of the constituent materials to evaluate E'. This value was found about 15% higher than the matrix Young's modulus. It should be noted that for a composite specimen, this formulation is considered realistic when the fiber spacing is small in comparison with the crack length. For the specimens used in this work, the fiber spacing is relatively large. Thus, the homogeneity assumption is not realistic. However, the comparison of the traction values obtained from this formalism with the experimental data from the FBG sensors and the numerical simulations is carried out in an average sense (Section 4).

While the calculation of the COD from known bridging tractions is rapid, the inverse calculation of the bridging function from a known COD often requires iterative, computationally expensive procedures. To perform the inverse calculation rapidly, one can make the simplification that the bridging traction is a piece-wise constant function,

$$\varphi(x) = \sum_{j=1}^{n} \varphi_j h_j(x), \qquad h_j(x) = \begin{cases} 1 & x_{j-1} \le x \le x_j, \\ 0 & x < x_{j-1} > x_j. \end{cases}$$

As long as the number of segments is chosen such that there are several segments per bridging fiber diameter, this assumption is reasonable. Further, as explained later, the COD was experimentally measured at a finite number of points along the length of the crack, thus these segments were chosen to correspond to the measurement points. This form of the bridging function allows one to separate the coefficients φ_j from the double integral, reducing Equation (1) to an equation in discrete form (see Appendix A for more details),

$$u(x_j) = u_\infty(x_j) - \frac{4}{E'} \left[\sum_{s=j+1}^{n} \sum_{k=1}^{s-1} \varphi_k \Omega_{jsk} + \sum_{s=j+1}^{n-1} \varphi_s \gamma_{sj} \right]. \tag{2}$$

The expressions for Ω_{jsk} and γ_{sj} are given in Appendix A. The matrices Ω_{jsk} and γ_{sj} depend only upon the specimen geometry and crack length thus, they can be calculated once for a given geometry and be stored for use with all future COD data. This significantly reduces the computation time and is the major advantage of this discretization technique. All integrations to evaluate the matrices given in Equation (2) were performed numerically.

Although the goal of this work is to determine the bridging tractions due to a few fibers, the technique used to measure the COD, described later, allows one to measure the COD at a large number of points. Thus, to reduce experimental errors, the COD was measured at 150 points and then a least-squares fit applied to obtain the bridging tractions. The COD $\overline{u}_j$, at each point x_j, is measured and the following vector $\overline{\mathbf{u}} = \{\overline{u_j}\}$, is formed. We want to minimize V, the difference squared between $\overline{\mathbf{u}}$ and $\mathbf{u}$, the COD calculated due to an assumed vector of bridging tractions φ:

$$\min_{\varphi} V = \sum_{j=1}^{n} \left[\frac{(\overline{u}_i - u_j)}{\overline{u}_j} \right]^2.$$

The problem is then reduced to solving the following matrix equation, as derived in Appendix A,

$$\mathbf{B}\varphi = \mathbf{f}. \tag{3}$$

The results obtained by this unconstrained least squares method can show numerical instabilities which appear as important oscillations. This was not considered to be important in this work, as the oscillations affected only a small number of points. Nevertheless, such oscillations can be removed by applying linear inequality constraints (Lawson and Hanson, 1974).

2.2. Finite element simulations

The actual specimen geometry and the loading conditions used in the experiments were modeled using a 3D Finite Element (FE) model in order to facilitate the experimental design and to obtain comparisons with the experimental results on bridging tractions and COD. Three dimensional models with an ideal crack as well, as with a non-zero initial crack opening, to model the artificial crack described in Section 3, were constructed. The essential parts of the mesh are presented in Figure 2. Due to the symmetry of the specimen and applied loads,

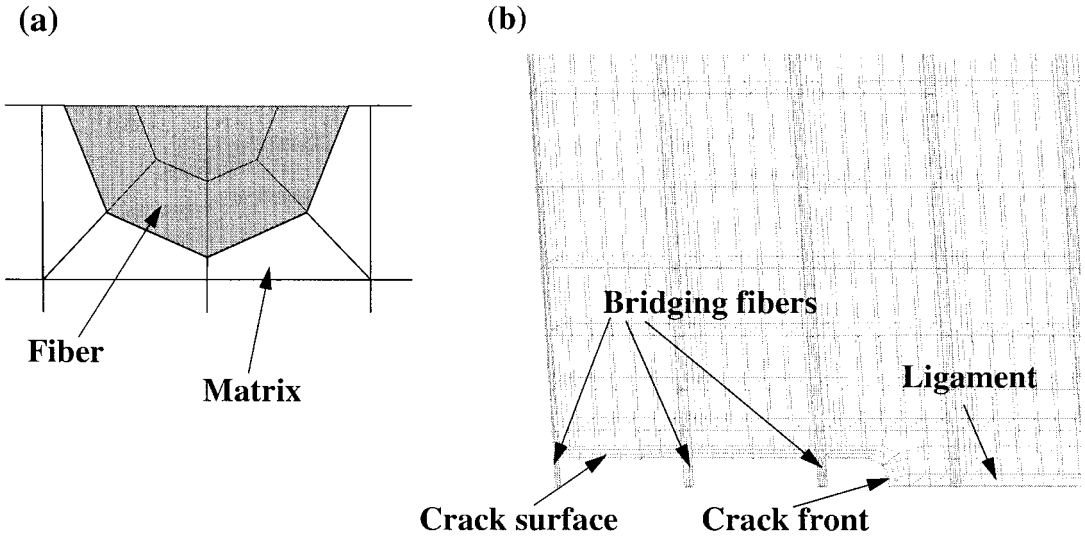

Figure 2. Typical meshes for the fiber and the specimen used to compare the experimentally measured tractions and COD profiles: (a) fibre intersection (b) specimen at the proximity of the crack.

only an eighth of the specimen was simulated with symmetric boundary conditions applied on the corresponding symmetry planes. Linear 8-node elements were used. The fibers were modeled as prisms with octagonal cross sections and the crack tip was approximated by a piece wise linear contour based on morphological observations. The crack length was chosen by examining the specimen before testing.

2.3. Optical fiber Bragg gratin

A Bragg grating in an optical fiber is a periodic change in the refractive index in the fiber core along a given length of the fiber. Exposing the silica fiber, doped for example with germanium and hydrogen, to UV light increases the index of refraction locally. Generally, Bragg gratings are introduced through the use of a phase mask during the UV exposure (Kashyap, 1999). The grating reflects a given wavelength of light (referred to as the Bragg wavelength) while transmitting other wavelengths. This reflection phenomenon is due to the coupling between forward and backward propagating modes in the fiber near the Bragg wavelength. When a broad spectrum is propagated in the fiber most of it is transmitted through the grating while a relatively small peak is reflected, as shown in Figure 3. The wavelength at maximum reflectivity, λ_B, is given by the expression,

$$\lambda_B = 2n_{\text{eff}}\Lambda.$$

Here, Λ is the period of the grating, and n_{eff} is the effective refractive index of the fiber core (Erdogan, 1997). If an axial strain is applied to the fiber, it will affect both Λ and n_{eff}, and hence λ_B. A temperature change also affects λ_B, but it is assumed here that the temperature remains constant throughout the experiments. The shift in wavelength $\Delta\lambda$, as a result of the change in grating period, is linearly related to the applied strain (Measures, 1992)

$$\frac{\Delta\lambda}{\lambda_B} = (1 - p_e)\varepsilon_{zz}, \tag{4}$$

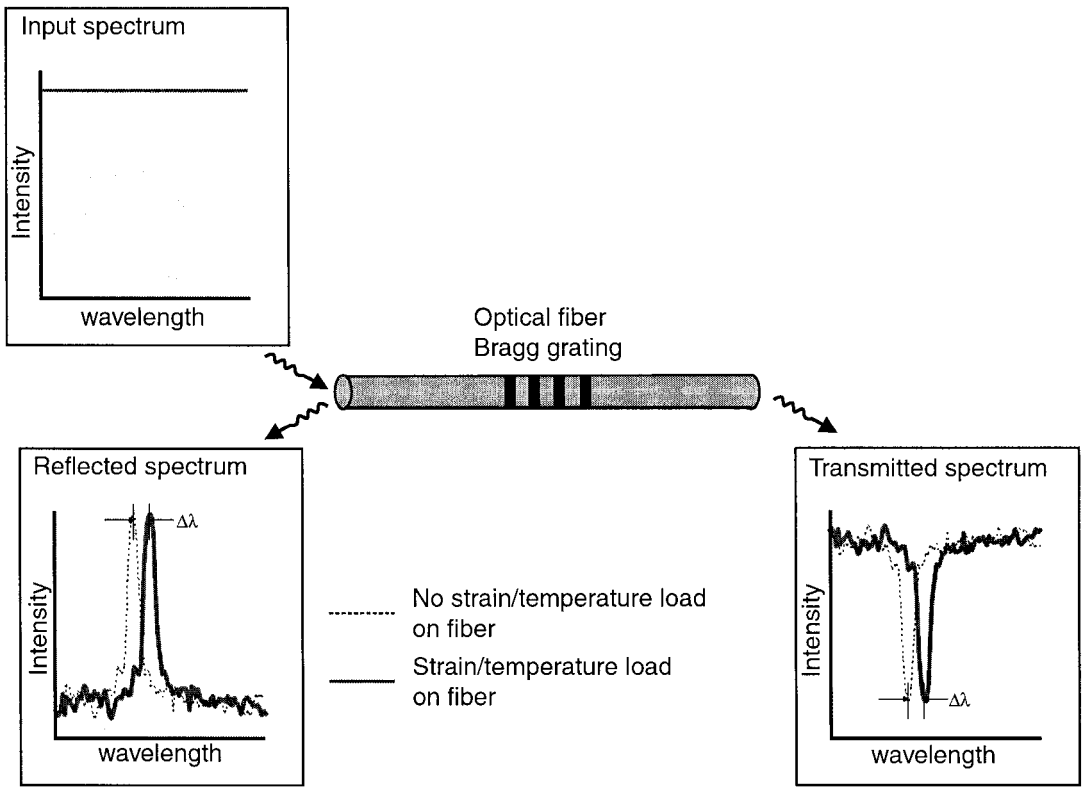

Figure 3. Principle of the optical Fiber Bragg Grating (FBG) sensor. A narrow peak of the input light is reflected by the Bragg grating, while other wavelengths are transmitted. When temperature or strain is applied to grating the reflected wavelength is shifted by $\Delta\lambda$.

where p_e is the photoelastic constant of the fiber and ε_{zz} the applied axial strain. Thus, the measurement of the shift of the reflected peak gives the strain in the fiber at the location of the grating. Assuming that the stress-strain behavior of the optical fiber is linear elastic, the axial force, F_f, in the fiber can be directly calculated from the axial strain as follows,

$$F_f = \frac{E_f A}{1 - p_e} \frac{\Delta\lambda}{\lambda_B}, \tag{5}$$

where A is the cross-sectional area of the fiber and E_f is the Young modulus of the fiber. While the response of a Bragg grating is easily calculated when the strain field is homogeneous, its response in a non-homogeneous strain field is generally solved using numerical methods (Erdogan, 1997). To invert the non-homogeneous strain distribution, iterative procedures can be applied (Peters et al., 2001).

3. Experimental procedures

In this work, optical fibers were used both as reinforcement and as strain sensors to directly measure forces on selected fibers bridging a crack. Simultaneously, the COD was measured along the crack as a function of the remote load. Thus, the tractions predicted by the weight function method can be compared with those obtained from the sensors. The experiments presented here are based on a quasi-static traction test on a model composite with one layer

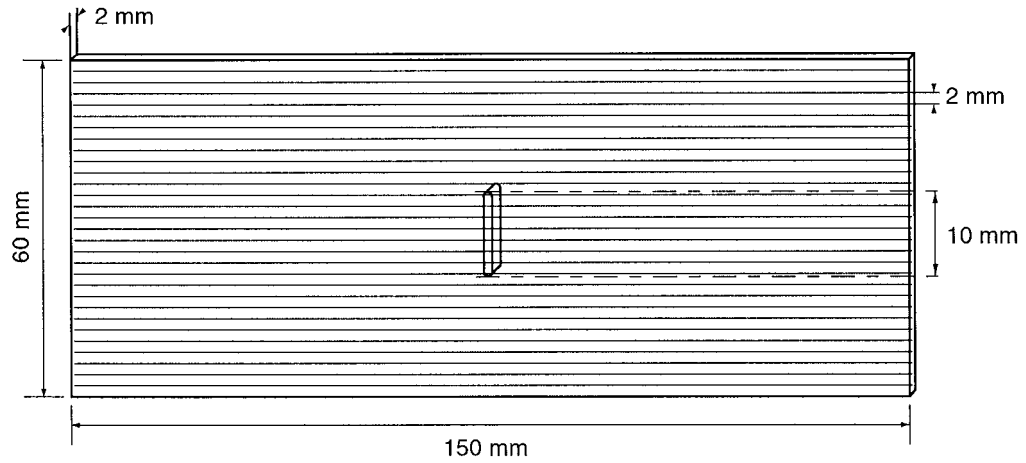

Figure 4. Geometry and dimensions of the center cracked specimen. The crack length is exaggerated for better clarity.

Table 1. Characteristics of the manufactured specimens

Specimen	S1	S2	S3	S4	S5
E_m (GPa)	2.74	2.59	2.96	2.78	2.91
No. of grated fibers	1	1	1	2	2
(Distance from center, mm)	(0)	(0)	(0)	(3)	(0, 4)
Length of Bragg Grating (mm)	036	0.38	0.17	0.36, 0.31	3*x* 0.17

of optical fibers. One or several fibers contained a Bragg grating located between the crack faces. This section explains the experimental procedures, including the specimen preparation, the experimental methods, and an estimation of the experimental error.

3.1. Specimen preparation

The specimens used in this work were Center Cracked specimens (CC) of dimensions 150 mm $\times$ 60 mm $\times$ 2 mm (Figure 4). The matrix was a three component epoxy (Dow Chemical Company), composed of DER 330, DER 732P and DEH 24 mixed in a 35:15:10 weight ratio. The Young's modulus of the epoxy, E_m, was measured independently and showed variations up to 6% (Table 1) which was attributed to small variations in the relative amount of the different resin components during mixing.

The reinforcing fibers were standard telecommunication optical fibers (Fibercore), with a diameter of 125 μm and a Young's modulus of $E_f = 72$ GPa (Carman and Sendeckyj, 1995). The polyamide coating of these fibers was removed using sulfuric acid (H_2SO_4, 96%) along the embedded length. To assure a strong interface, the fibers were then treated with silane (A1100 Union Carbide Corporation) and dried for 24 hours in an appropriate recipient. The fiber(s) containing the Bragg grating(s) had an additional plastic coating at the exit points from the specimen, to avoid breaking during specimen handling. The gratings on the

fibers (Table 1) were written at the Institute of Applied Optics (Swiss Federal Institute of Technology, Lausanne, Switzerland).

The fibers were placed in the mold, spaced 2 mm apart, under a slight tension to assure that they were parallel and well aligned. Care was taken so that the grating(s) was symmetrically located with respect to the middle plane of the specimen, normal to the fibers. Epoxy was then added, after being placed in a vacuum to remove air bubbles, and was allowed to cure for at least 24 hours. When removed from the mold, the specimen was machined to the appropriate dimensions. The grating was located along the fiber using Optical Low Coherence Reflectometry (HP 8504B precision reflectometer), with a precision of 500 μm. The latter measurement helped to ensure that the FBG was located between the crack faces.

The central, 10 mm long, crack was introduced using a three step procedure. First, epoxy was removed using a saw up to a depth of 0.7 mm on each side of the specimen. Second, an UV excimer laser (Lambda Physics LPX61oi, 308 nm excimer laser for ablation-deposition, 2 J cm^{-2} energy, pulses of 250 ns) was utilized to cut through the specimen. This particular wavelength is well absorbed by the epoxy, which evaporates instantly, while not absorbed by the glass fibers, which remain intact. The specimen was irradiated during 4 to 5 hours at a frequency of 5 Hz. Finally, the epoxy residue, within the artificial crack, was removed with sulfuric acid in order to obtain a clean crack of about 1 mm wide. All specimens were examined under a microscope before testing in order to examine the crack tip geometry and to measure the crack length, the fiber spacing, and their distances from the crack tips. The crack tip shapes were not well controlled. However, in all specimens, except one, the FBGs were relatively far from the crack tips so that the tip shape influence on the fiber strain measurements was considered negligible.

In this work, the results from five specimens are reported. The corresponding specimens are named S1 to S5. In specimens S1 to S3, five fibers bridged the crack while in S4 four fibers bridged the crack. In S5 there were only three bridging fibers. The geometry of these specimens was identical, however, the number of fibers with gratings was different: in S1 to S3 the central fiber contained a grating while in S4 and S5 two fibers contained gratings. The specifications of all specimens are listed in Table 1.

3.2. Experimental methods

The specimens were tested in quasi-static tension in a pressure controlled hydraulic loading device fabricated in house (Figure 5). The specimen was held by flat grips tightened with screws. The imposed pressures resulted in loading steps of 10 to 50 N. A load cell, connected along the displacement axis, measured the applied force at the grips. A LVDT gave the position of the driving shaft. An ESPI unit was used for simultaneous measurements of the surface displacements (Jones and Wykes, 1989) on the specimen at each loading step, in order to determine the COD. The ESPI setup was configured to make measures of displacements in the direction of loading as shown in Figure 6. The laser used was a HeNe at wavelength of 632 nm. From the displacement field obtained, a contour line was taken near the crack to directly deduce the COD. The sensitivity, d, of the measurement depends on the wavelength of the laser, λ, and the angle of inclination between the beams and specimen surface, θ (see Figure 6),

$$d = \frac{\lambda}{2\ \sin(\theta)}. \tag{6}$$

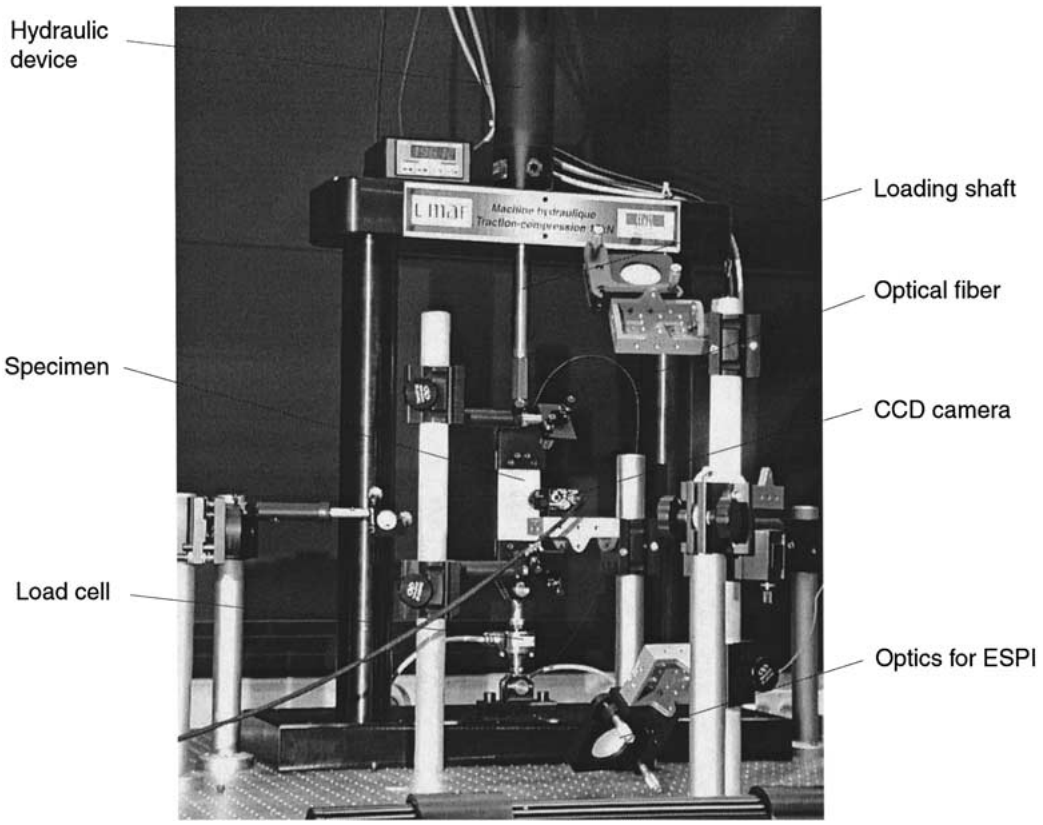

Figure 5. Loading device and some of the ESPI optical elements, supported on a vibration-isolated table. The exiting optical fiber, which contains a Bragg grating, is also visible.

In the setup used, the sensitivity between two displacement fringes was $d = 0.49\ \mu$m. Since this technique is very sensitive to vibrations, and because the measurements are normally taken at relatively long time intervals, the loading frame and the entire optics system were mounted on a vibration-isolated table.

In each experiment, the FBG was connected on one side to a tunable laser (Tunics 155 nm, Photonetics) and on the other side to a photodetector, in order to measure the transmitted spectrum of the grating. The acquisition of the spectra was performed using a LABVIEW program to control the tunable laser and the intensity measurements. Some of the spectra were measured in reflection using a 50-50 fiber coupler, due to fiber breakage at one end of the specimen. However, this did not affect the calculated strain.

As observed in previous experiments (Peters et al., 2001), the relationship between the shift of the peak and the strain in the fiber was linear and the value of $(1 - p_e)$ was calibrated for each of the fibers used. The calibration of $(1 - p_e)$ yielded 0.74 ± 0.02 for specimen S1, S2 and S4 and 0.76 ± 0.01 for the other specimens. The reproducibility of the spectra and FBG strains were examined through the results of the S1 to S3 specimens and supported by numerical simulations of the actual specimens. Relevant discussion is presented in Section 4.

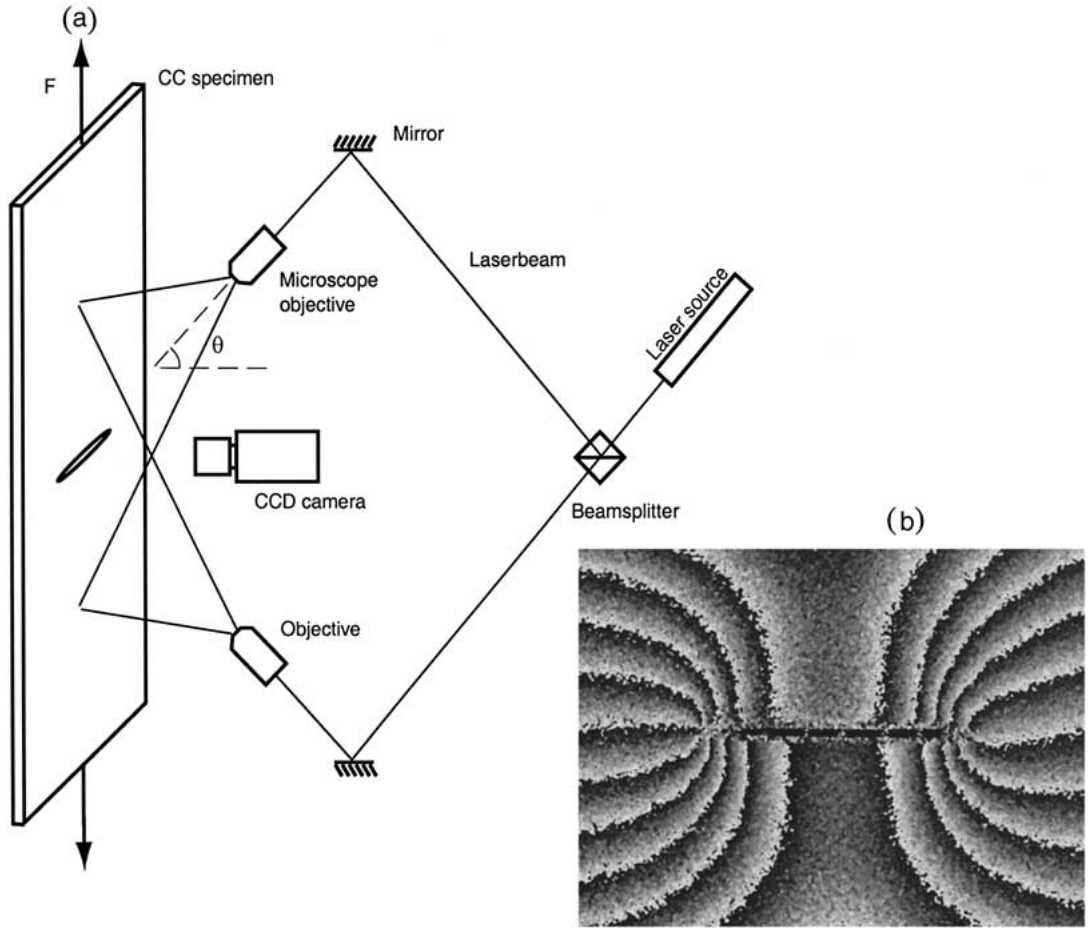

Figure 6. (a) Experimental set-up of Electronic Speckle Pattern Interferometry (ESPI) used in experiments; drawing not to scale. (b) Example of equivalent vertical displacement fringes around a crack due to a vertical force F. Each fringe corresponds to a displacement step of 0.49 μm.

3.3. Error estimation

To determine the effect of variations in the material properties, the specimen geometry, and the measurement precision on the results, an error estimation was performed. The applied force, F_∞, at the grips was indicated by the load cell with a precision of ± 0.5 N and the position of the peaks of the spectra were measured with a precision of ± 0.05 nm. These errors are normally reduced by the curve fitting of the data on strains on the fiber plotted against F_∞ and as they are very small, they were neglected. Also the errors due to the variation in the photoelastic constant, the fiber diameter and the elastic constants of the fibers were on the order of 4%. Therefore, any error on the data comes primarily from differences between the specimens. In this work, it was assumed that the total error is the addition of errors due to the specimen geometry and material properties. Namely, the Young's modulus of the epoxy, E_m, the position of the grated fiber with respect to the center of the crack, x, and the crack size, a.

To estimate the error on F_f due to variations in the specimens, one solves Equation (1) for the central crack configuration (at a constant applied force) (Tada et al., 2000). Thus, the error

Table 2. Results of measured and calculated forces for a 1N remote loading force

Specimen	S1,S2,S3	S4 A	S4 B	S5 A	S5 C
Distance from the center (mm)	0	3	3	0	4
Measured forces F_f (N)	0.0176	0.0145	0.0138	0.0220	0.0109
Error ΔF_f (N)	0.0029	0.0025	0.0024	0.0009	0.0017
Forces from 2D weight function COD analysis (N)	0.0172	0.0136	0.0136	0.0132	0.0175
Forces from 3D numerical simulations (N)	0.0164	0.0143	0.0143	0.0181	0.0131

on the force in the fiber due to the specimen geometry and the matrix Young's modulus, E_m, becomes

$$\frac{\Delta F_f}{F_f} = \left|\frac{\Delta E_m}{E_m}\right| + \left|\frac{\Delta a}{a}\right| \frac{1}{(1 - x^2/a^2)} + \left|\frac{\Delta x}{x}\right| \frac{1}{(a^2/x^2 - 1)}. \tag{7}$$

For the material properties used herein, the sum of these two errors is given in Table 2. An additional possible source of error not considered above is the positioning of the grating between the two crack faces. As the position of the grating is measured with a precision of 500 μm and since the crack width is less than 1 mm, part of the grating may be in the matrix material and thus, affect the force measurements. Moreover, when embedded in epoxy, the grating shows a change in the form of the transmitted spectrum such as the appearance of secondary peaks and a diminution of the depth of the principal peak. This is due to transverse forces applied to the fiber grating as a result of residual stresses in the epoxy (Peters et al., 2001). However, no such changes were observed in the obtained spectra thus, one can deduce that the grating(s) was within the crack faces.

4. Results and discussion

Figure 7a shows the specimen S3, with a magnification of the crack (Figure 7b) and one of the bridging fibers (Figure 7c) containing a Bragg grating. The crack faces were clean when viewed at the level of magnification indicated in Figure 7. In all specimens, a thin yellow layer of epoxy material was observed along the crack faces and attributed to the exposure of the epoxy to the laser during the cutting process. This may influence the epoxy elastic constants locally, but as it extended over a very thin surface layer, it does not affect the results of the force measurements. This assumption is supported by the agreement with the numerical simulations discussed later. Note also that the distances of the fibers close to the crack tips are not the same at both ends. This is due to a lack of precise horizontal placement of the artificial crack. The holes in the specimen are for the screws used to tighten the specimens in the grips.

Quasi-static tests in traction were performed within the linear loading range of the epoxy and below the specimen crack propagation load. At each loading step, the transmitted spectrum of the grating(s) was measured. A typical set of spectra, taken from specimen S2, is shown in Figure 8 for five levels of the remote load. These spectra clearly show that the depth of the principal peak is constant and that the spectra have similar shapes. This indicates that the grating was between the crack faces and thus the strain along its length is uniform. The

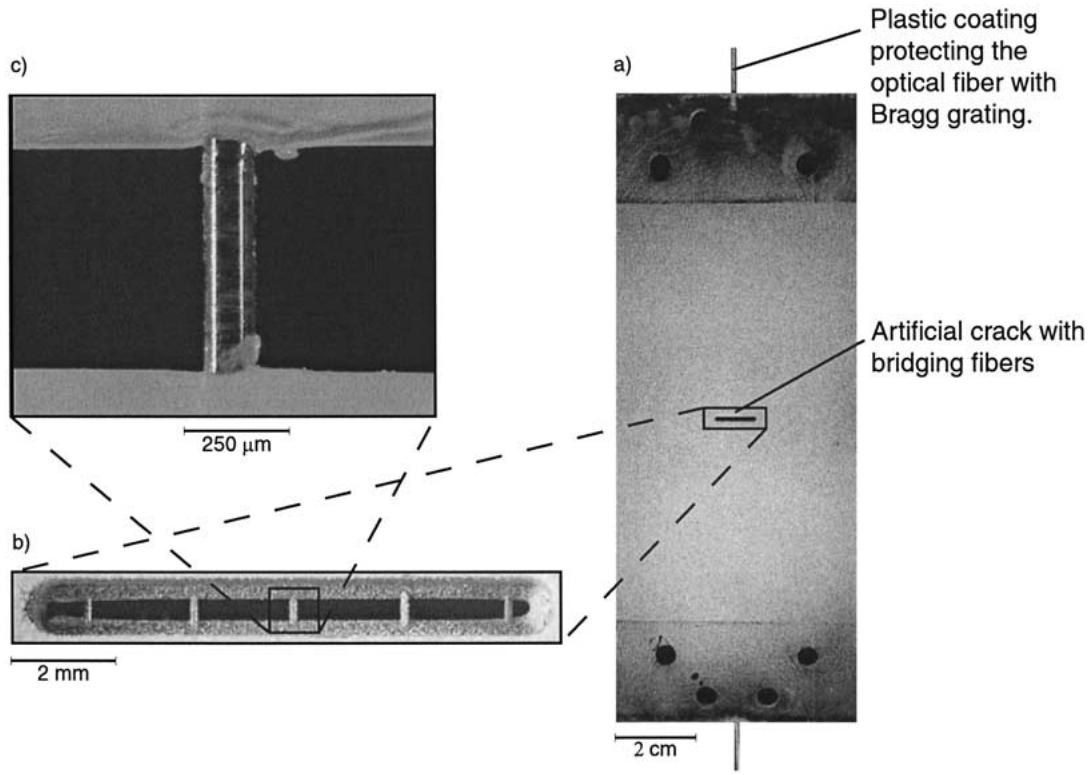

Figure 7. (a) Photograph of an actual specimen; (b) magnification of the crack; (c) one of the bridging fibers. The two white lines on the fiber seen in (c) are reflections of external lighting.

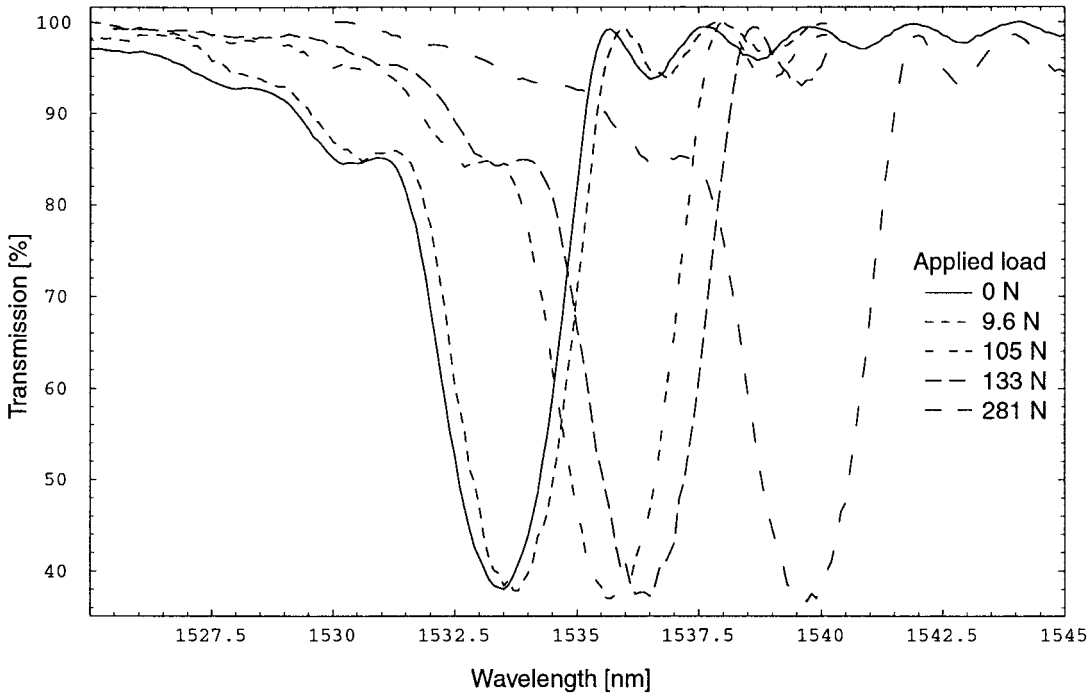

Figure 8. Measured spectra from traction test for specimen S2 at several load levels. One can see the wavelength shift due to strain.

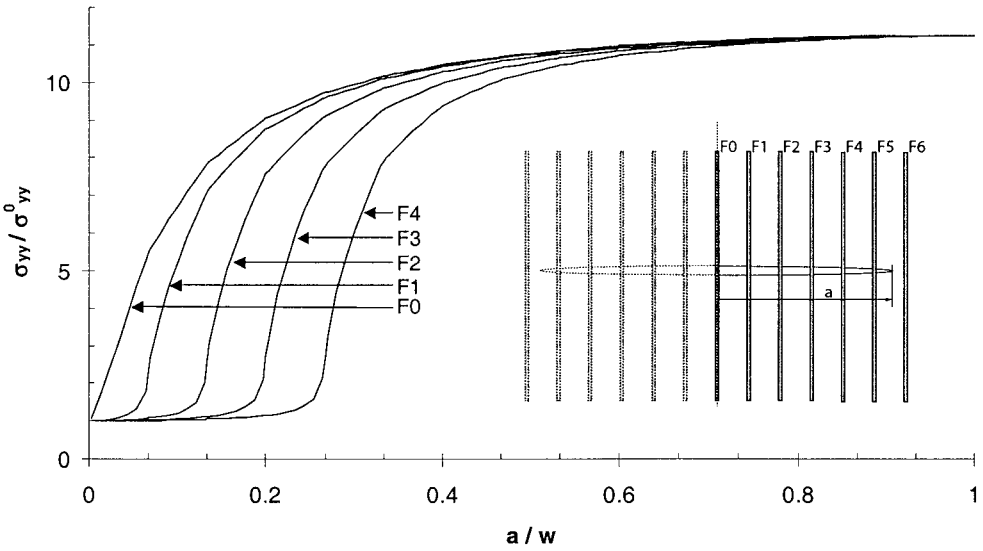

Figure 9. Normalized vertical stress, σ_{yy}, on 5 bridging fibers, indicated as F0–F4, presented as a function of the normalized crack length determined with a 3D numerical model. σ^0_{yy} refers to the fiber stress on the uncracked specimen.

small extent of asymmetry in the transmitted spectrum is attributed to the manufacturing of the grating.

To support the experimental design and the results on the fiber bridging forces and COD, 3D linear elasticity finite element simulations were performed with the specimen geometry and material properties used in the experiments. Since the fibers were treated with silane, a perfect fiber-matrix interface was considered. First, a set of simulations was performed in order to examine the forces on the fibers as a function of the crack length using a zero initial COD. Results of such simulations for the five bridging fiber forces are presented in Figure 9. The force on a typical bridging fiber reaches a constant value after a certain crack-tip fiber distance. For this particular geometry the minimum distance is about five times the fiber spacing. Note also the high rate of change in the traction on a bridging fiber when it is located right behind the crack tip. The second set of simulations was performed for the fiber forces and the COD accounting for the actual crack geometry and applied load recorded experimentally. Results of these simulations are presented later in this section.

Using the experimental data, the forces in the fibers containing Bragg gratings were calculated from the measured wavelength shift Equation (5) and are plotted as a function of the remote load for each specimen in Figures 10–12. For each set of data, the crack geometry and fibers are shown in an insert on the corresponding Figure. Note that all experimental data are linear as a function of remote load.

The force on the central fiber, as a function of the remote load is plotted in Figure 10. The data in Figure 10 show three different slopes corresponding to specimens S1, S2, and S3. For comparison, the average slope is also plotted in Figure 10. In this series of experiments, a 15% difference was observed between the slopes of S1 and S3 and an average value of 0.0176. These differences are within the specimen manufacturing errors, as described in Section 3.3, and are listed in Table 2. Additionally, the results of the finite element simulations are within 7% of the average values obtained experimentally.

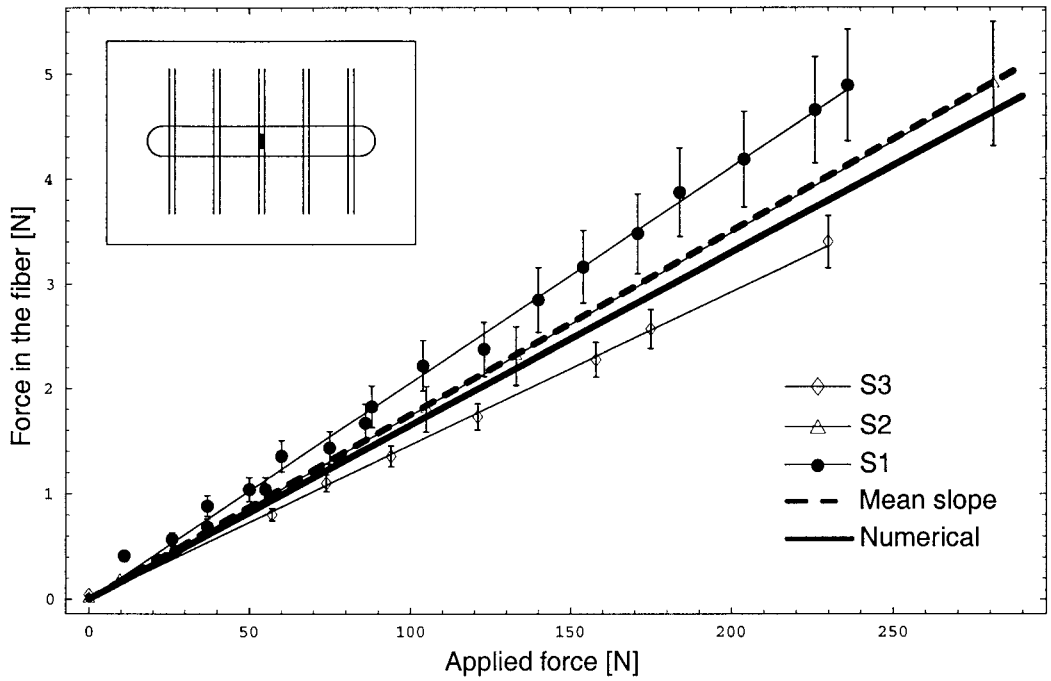

Figure 10. Forces measured in the central fibers for three different specimens as a function of the applied load. Both experimental data and linear fit are plotted. Also shown are results of numerical simulations. Insert shows crack - fiber configuration.

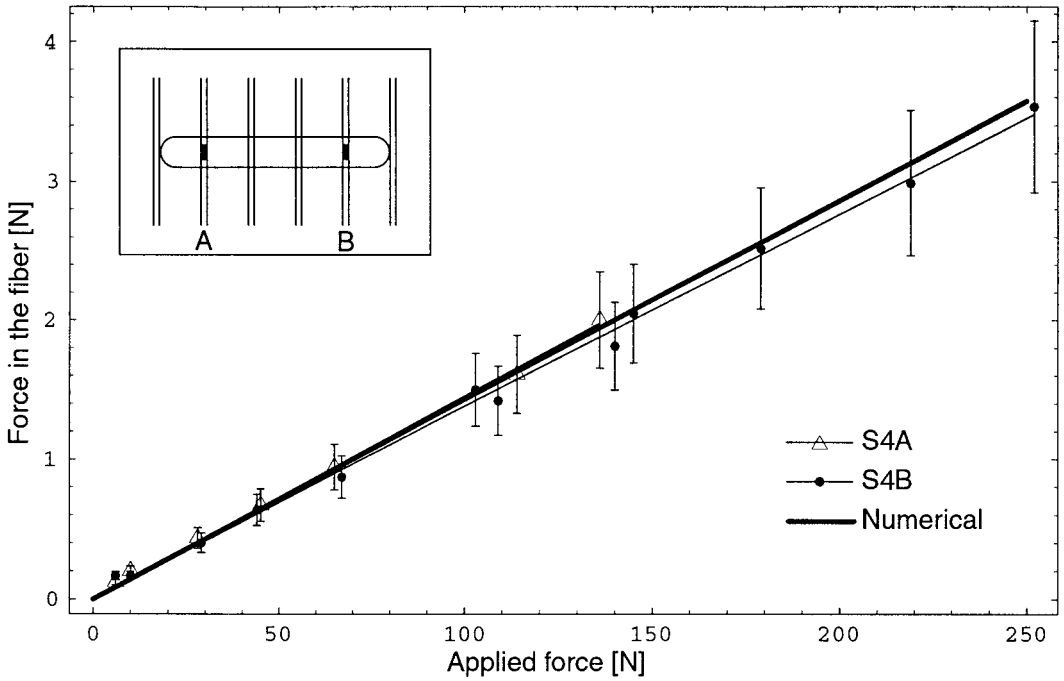

Figure 11. Forces measured in two fibers of the same specimen at symmetric locations as a function of the applied load. Both experimental data and linear fit are plotted. Also shown are results of numerical simulations. Insert shows crack-fiber configuration.

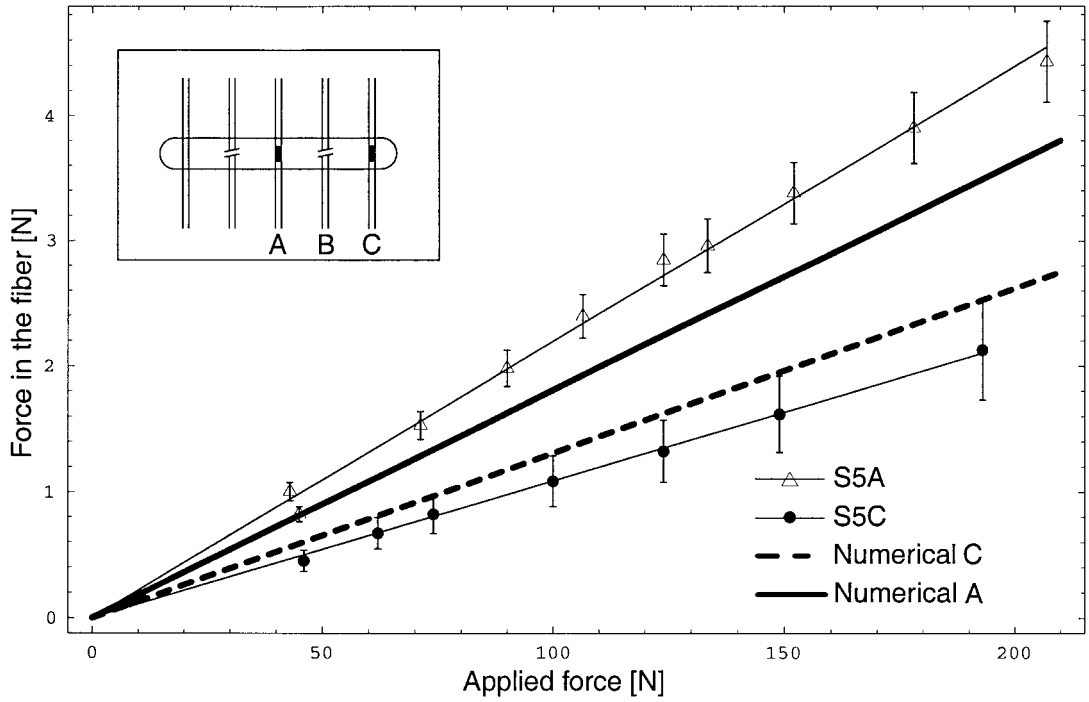

Figure 12. Forces measured in two fibers on the same specimen at different locations as a function of the applied load. Both experimental data and linear fit are plotted. Also shown are results of numerical simulations. Insert shows crack-fiber configuration.

The forces on the two fibers of specimen S4 are shown in Figure 11. Note here that the difference in these forces was within 5%. This close result was expected since these fibers are located the same distance from the crack center. The small difference also confirmed that most of the error observed in the data of Figure 10 was due to differences between specimens. Also shown in Figure 11 are the results of the numerical simulations using four bridging fibers. As in the case of Figure 10, the experimental data and the simulations are very close.

Similar measurements from specimen S5 are shown in Figure 12. Here, two fibers (see insert on Figure 12) fractured during the fabrication process which was later taken into account in the analysis. Note that the measured force on the fiber closest to the crack tip is smaller (about half) than the force supported by the central fiber. Although this trend is observed in the numerical studies of an ideal crack (Figure 9), the forces obtained from the 3D numerical simulations of the exact specimen geometry with a central fiber and two fibers at 1 mm from each crack tip differ from the experimental values by about 19% in opposite sense (Table 2). Morphological observation on this specimen, showed a distance of the crack tip and the closest fiber of about 0.8 mm. Numerical results indicated that a change in the distance between the fiber and the crack tip by 20% resulted in a 25% change on the fibre force (Figure 9). Thus, the observed differences in the experiments and simulations using 1 mm distance (Figure 12) were attributed to the variations in the distances used in the simulations and the experimental one.

For each specimen tested, ESPI images of the specimen surface displacements were also taken at each loading step. The unwrapped images were added and a path was chosen around the crack as close as possible to the crack faces from which the COD was determined. The

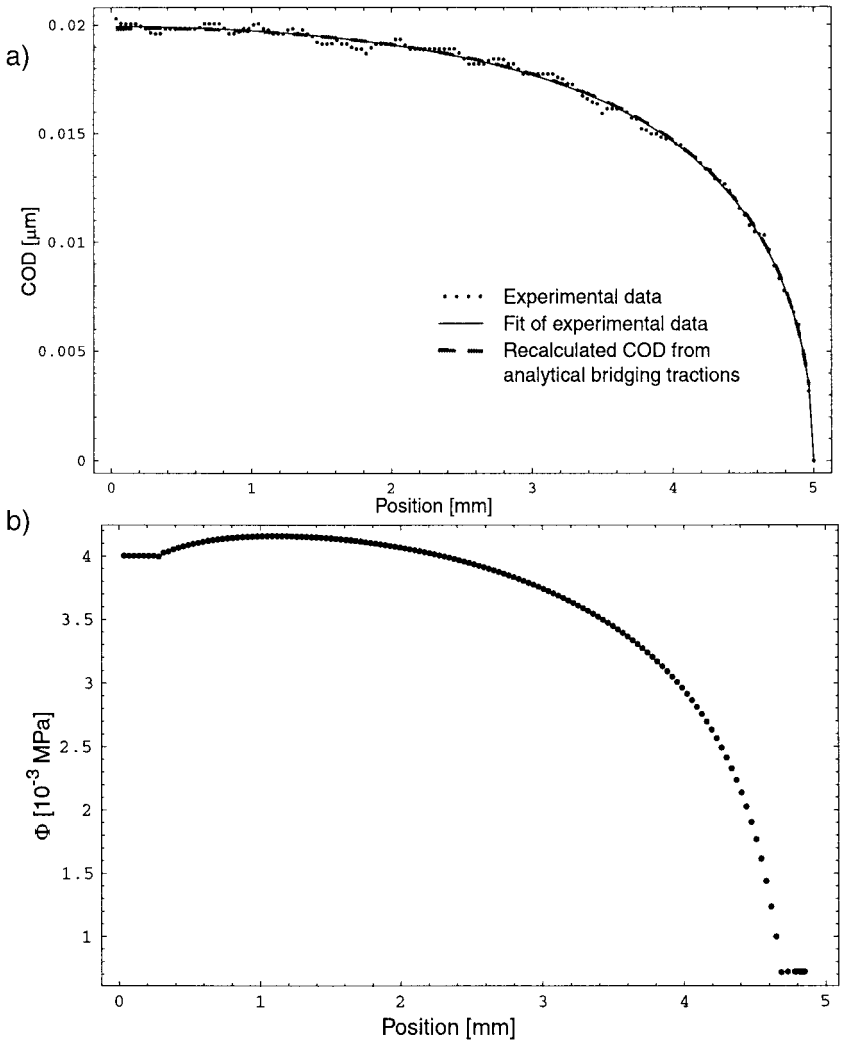

Figure 13. (a) Measured and calculated COD. (b) Calculated pressure distribution along the half-crack corresponding to the measured COD shown in (a). From this pressure distribution, a COD was calculated, and compared with the measured one (a) (see text for details).

COD of specimen S3, per 1N applied force, is shown in Figure 13a. It should be pointed out that the weight function method for determining bridging tractions using experimental COD data, is very sensitive to small variations in the COD measurements. Especially for points near the crack tip, a small change of the COD significantly affects the value of the bridging tractions along at least a third of the crack length. Also a small rotation of the specimen during loading can modify the shape of the COD and thus, the calculated bridging tractions. The measured COD profiles were fitted using a polynomial to eliminate the local variation of the COD which was due to noise.

Using the scheme presented in Appendix A, the 2D bridging stress distribution was calculated for all five specimens using Equations (1)–(3). The traction distribution for specimen S3 is shown in Figure 13b for a half-crack. A small number of points near the center of the specimen and close to the crack tip showed oscillations due to the analytical method and

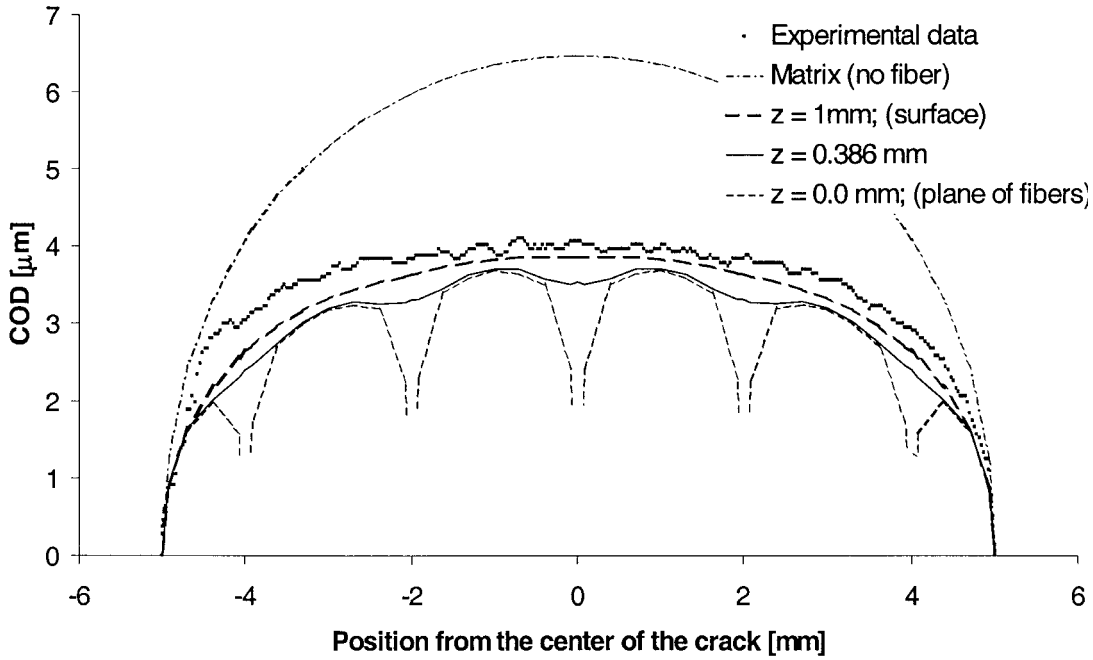

Figure 14. Crack opening displacement for three distances from the specimen surface (specimen thickness 2 mm). Both numerical simulation and experimental data are plotted.

have been replaced with an average value. To check for consistency of the numerical scheme for the bridging tractions, the COD was calculated using the determined tractions. As can be seen in Figure 13a, the calculated COD profile was practically identical to the one measured experimentally thus, demonstrating the accuracy of the ESPI measurements combined with the weight function approach for determining the corresponding bridging stress distributions.

Experimental data on the COD were also compared with 3D numerical simulations of the actual load - specimen configuration. Figure 14 shows COD profiles evaluated experimentally on the surface of the specimen and calculated numerically at three different planes. Note the good agreement of the experimental measurements and the numerically obtained values (at the surface). The numerical simulations demonstrate that a significant change in the COD profiles due to the presence of the fibers commences at about a third of the specimen thickness. Therefore, the surface effect due to the finite diameter of the bridging fibers cannot be seen for the particular geometry used. The measured bridging tractions are distributed over the length of the crack.

Finally, to compare the tractions obtained from the 2D COD-weight function data with the 3D experimental and numerical simulations, the 2D tractions were integrated over the crack's surface in order to determine statically equivalent closing forces at the location of the fibers. For the specimens S1–S4, the integral was extended over a fiber spacing and the results are shown in Table 2 with the experimental data from the FBG and the numerical simulations. The weight function method, although limited by the 2D approximation, gave very good results.

Similar comparisons were carried out for the data of specimen S5 (Table 2). For this specimen, it was difficult to compare the COD-weight function data on the farces and the ones from the FBG since only three bridging fibers were intact. However, the consistency of the experimental results and analysis is easily seen if we compare the total force on the

crack races obtained from the COD-weight function data with the ones from the FBG and the numerical simulations (Table 2).

5. Conclusions

A new experimental technique for direct non-invasive measurements of bridging forces in a glass-fiber/epoxy composite is presented. The main advantage of this method is that it can be used in real, non-transparent composites. The measurements of bridging forces using FBG sensors were precise, as long as the geometry of the specimen and the interface between the fibers and the matrix were well controlled. The measurement of the COD using ESPI also showed a good precision, and the large number of measured points in this method was very useful for determining bridging tractions. Although a 3D weight functions could be used in a similar manner to obtain the tractions, the calculation of bridging stress profile using 2D weight function method was in good agreement with the measured and the numerical values, as long as the fibers are not to close from the crack tip. This work can be continued to include more fibers in the bridging zone. Also a distributed measurement of the forces along the bridging fibers is possible when using long gratings traversing the crack and entering the epoxy. This could give informations on the interface between the fiber and the matrix and, for a weak interface, on debonding.

Acknowledgements

The authors wish to acknowledge the financial support of the Swiss National Science Foundation, through grants FN 21-50549.97 and FN 20-56871.99. Thanks are also due to Frank Wagner, IOA-EPFL, who performed the laser cutting and to Prof. Salathé and Dr H. Limberger for useful discussions. The testing apparatus was designed at the machine shop of the institute with the help of Gino Crivellari and Marc Jeanneret. Their help is gratefully appreciated.

Appendix A

Formulation of crack opening displacement and bridging tractions

The problem considered is that of a two dimensional crack in a homogeneous material (with effective Young's modulus E') and subjected to remote loading, σ_∞, and bridging tractions, $\varphi(x)$ (see Figure 1). The goal is to calculate the bridging tractions from a known COD. Divide the interval $x = [0, a]$ into $n - 1$ segments such that $x_j = aj/n$. Assume that the bridging traction, $\varphi(x)$, is a piecewise constant function,

$$\varphi(x) = \sum_{j=1}^{n-1} \varphi_j h_j(x),$$

where $h_j(x)$ is the step function.

$$h_j(x) = \begin{cases} 1 & x_{j-1} \le x \le x_j, \\ 0 & x < x_{j-1}, x > x_j. \end{cases}$$

Thus, the problem is reduced to determining the vector $\varphi = \{\varphi_j\}$ $(j = 1, \ldots, n-1)$. The crack opening displacement (COD) $u(x)$, as a function of the bridging tractions is given by

$$u(x) = u_\infty(x) - \frac{4}{E'}\int_x^a \left[\int_0^{a'} g(x', a', w)\varphi(x')\,\mathrm{d}x'\right] g(x, a', w)\,\mathrm{d}a',$$

$$u_\infty(x) = \frac{4}{E'}\int_x^a \left[\int_0^{a'} g(x', a', w)\sigma_\infty(x')\,\mathrm{d}x'\right] g(x, a', w)\,\mathrm{d}a',$$

where $u_\infty(x)$ is the COD due to the remote loading and can be calculated independent of the bridging tractions. The function $g(x, a, w)$ is a known influence function dependent upon the specimen geometry. $u_\infty(x)$ is thus determined at each $x_j (j = 1, \ldots, n)$ and stored as the vector $\mathbf{u}_\infty = \{u_\infty(x_j)\}^T$. Substituting the piecewise constant form of $\varphi(x)$ into the expression for $u(x)$, one can write,

$$\int_0^{a'} g(x', a', w)\varphi(x')\,\mathrm{d}x' = \sum_{j=1}^{M(a')} \varphi_j \int_{x_{j-1}}^{x_j} g(x', a', w)\mathrm{d}x' + \varphi_{M(a')+1}\int_{x_{M(a')}}^{a'} g(x', a', w)\,\mathrm{d}x',$$

where $M(a')$ is the largest integer such that $x_{M(a')} \le a'$. The integral $\displaystyle\int_{x_{j-1}}^{x_j} g(x', a', w)\mathrm{d}x'$ is independent of the bridging tractions. Define the vector $\mathbf{f}(a', w)$ as

$$f_j(a', w) \equiv \int_{x_{j-1}}^{x_j} g(x', a', w)\,\mathrm{d}x'.$$

Combining, one can write,

$$u(x) = u_\infty(x) - \frac{4}{E'}\int_x^a \left\{\sum_{k=1}^{M(a')} \varphi_k f_k(a', w) + \varphi_{M(a')+1}\int_{x_{M(a')}}^{a'} g(x', a', w)\,\mathrm{d}x'\right\} g(x, a', w)\,\mathrm{d}a'.$$

Evaluating $u(x)$ at the data points $x_j (j = 1, \ldots, \frac{n-1)}{n}$ and dividing the interval $[x_j, a]$ into smaller segments yields,

$$\begin{aligned} u(x_j) = {} & u_\infty(x) - \frac{4}{E'}\left\{\sum_{s=j+1}^{n}\int_{x_{s-1}}^{x_s}\sum_{k=1}^{s-1}\varphi_k f_k(a', w)g(x_j, a', w)\,\mathrm{d}a'\right. \\ & \left. - \sum_{s=j+1}^{n}\int_{x_{s-1}}^{x_s}\varphi_s\left\{\int_{x_{s-1}}^{a'} g(x', a', w)\,\mathrm{d}x'\right\} g(x_j, a', w)\,\mathrm{d}a'\right\}. \end{aligned}$$

Changing the order of integration and summation in the first term leads to

$$\sum_{s=j+1}^{n}\int_{x_{s-1}}^{x_s}\sum_{k=1}^{s-1}\varphi_k f_k(a', w)g(x_j, a', w)\,\mathrm{d}a' = \sum_{s=j+1}^{n}\sum_{k=1}^{s-1}\varphi_k\int_{x_{s-1}}^{x_s} f_k(a', w)g(x_j, a', w)\,\mathrm{d}a'.$$

The integral on the right hand side is only dependent upon the specimen geometry and thus, can be calculated once for a given geometry and stored in the matrix form,

$$\Omega_{jsk} \equiv \int_{x_{s-1}}^{x_s} f_k(a', w)g(x_j, a', w)\,\mathrm{d}a'.$$

Similarly, we define the matrix γ such that

$$\gamma_{sj} \equiv \int_{x_{s-1}}^{x_s} \left\{ \int_{x_{s-1}}^{a'} g(x', a', w)\, \mathrm{d}x' \right\} g(x_j, a', w)\, \mathrm{d}a',$$

which, like Ω, is only a function of the specimen geometry. Collecting terms, the COD at the data points becomes,

$$u(x_j) = u_\infty(x_j) - \frac{4}{E'} \left[\sum_{s=j+k}^{n} \sum_{k=1}^{s-1} \varphi_k \Omega_{sjk} + \sum_{s=j+k}^{n-1} \varphi_s \gamma_{sj} \right].$$

LEAST-SQUARES FIT

Define the set of experimental COD data, taken at each point x_j, to be $\overline{\mathbf{u}} = \{u_j\}$. To make a least-squares fit to the data, one needs to minimize V, the difference squared between $\overline{\mathbf{u}}$, the data, and $\mathbf{u}$, the COD calculated due to the vector of bridging tractions, φ (as given above). Further, each term of the function V is weighted by $\overline{u}_j$ to prevent certain data points from dominating the results. Note that the minimization is performed with respect to φ,

$$\min_{\varphi} V = \sum_{j=1}^{n} \left[\frac{(\overline{u}_j - u_j)}{\overline{u}_j} \right]^2.$$

Now, define the vector $\mathbf{a} = \overline{\mathbf{u}} - \mathbf{u}_\infty$, and substitute the expression for $u_j = u(x_j)$ such that V becomes

$$V = \sum_{j=1}^{n} \frac{1}{\overline{u}_j^2} \left[a_j + \frac{4}{E'} \left(\sum_{s=j+1}^{n} \sum_{k=1}^{s-1} \varphi_k \Omega_{jsk} + \sum_{s=j+1}^{n-1} \varphi_s \gamma_{sj} \right) \right]^2.$$

By expanding the double sum containing Ω and then reducing, one can show that,

$$\sum_{s=j+1}^{n} \sum_{k=1}^{s-1} \varphi_k \Omega_{jsk} = \sum_{k=1}^{n-1} \varphi_k \sum_{s=\mathrm{Max}(j+1,k+1)}^{n} \Omega_{jsk}.$$

Now, define the matrix α (which does not depend on the bridging tractions) as

$$\alpha_{jk} \equiv \frac{4}{E'} \left[\sum_{s=\mathrm{Max}(j+1,k+1)}^{n} \Omega_{jsk} + \begin{cases} 0 & \text{if } k \le j \\ \gamma_{kj} & \text{if } k > j \end{cases} \right].$$

Thus one can write

$$V = \sum_{j=1}^{n} \frac{1}{\overline{u}_j^2} \left[a_j + \sum_{k=1}^{n-1} \alpha_{jk} \varphi_k \right]^2.$$

The matrix α can be assembled once for a given specimen geometry and stored. Now, minimizing V with respect to the vector φ reduces the problem to solving the equation,

$$\mathbf{B}\,\boldsymbol{\varphi} = \mathbf{f}$$

for the vector φ, where B is the $n \times n - 1$ matrix,

$$B_{ij} = \sum_{k=1}^{n} \frac{\alpha_{ki}\alpha_{kj}}{\overline{u}_k^2}$$

and f is the $n-1$ vector,

$$f_i = -\sum_{k=1}^{n} \frac{a_k\alpha_{ki}}{\overline{u}_k^2}.$$

References

Aveston, J., Cooper, G. and Kelly, A. (1971). *The properties of Fiber Composites, Proceedings National Physical Laboratory*, IPC Science and Technology Press Ltd., Guilford, U.K.

Belnap, J.D. and Shetty, D.K. (1998). *Composites Science and Technology* **58**, 1763.

Buchanan, D.J., John, R. and Johnson, D.A. (1997). *International Journal of Fracture* **87**, 101.

Bueckner, H.F. (1970). *Zeitschrift für Angewandte Mathematik und Mechanik* **50**, 529.

Budiansky, B., Hutchinson, J.W. and Evans, A.G. (1986). *Journal of the Mechanics and Physics of Solids* **34**, 167.

Budiansky, B. and Amazigo, J.C. (1989). *Journal of the Mechanics and Physics of Solids* **37**, 93.

Carman, G.P. and Sendeckyj, G. (1995). *Journal of Composites Technology and Research* **17**, 183.

Chen, C-H. and Chang, P.-R. (1997). *Mechanics of Materials* **25**, 47.

Cox, B.N. and Marshall, D.B. (1991). *International Journal of Fracture* **49**, 159.

Erdogan, T. (1997). *Journal of Lightwave Technology* **15**, 1277–1294.

Jones, R. and Wykes, C. (1989). *Holographic and Speckle Interferometry*, Cambridge University Press, Cambridge.

Kashyap, R. (1999). *Fiber Bragg Gratings*, Academic Press, San Diego.

Lawson, C.L. and Hanson, R.J. (1974). *Solving Least Squares Problems*, Prentice-Hall, Englewood Cliffs.

Marshall, D.B., Cox, B.N. and Evans, A.G. (1985). *Acta Metallurgica* **33**, 2013.

McCartney, L.N. (1987). *Proceeding of the Royal Society of London* **A409**, 329.

Measures, R. (1992). *Composites Engineering* **2**, 597.

Nemat-Nasser, S. and Hori, M. (1987). *Mechanics of Materials* **6**, 245.

Peters, K., Studer, M., Botsis, J., Iocco, A., Limberger, H. and Salathé, R. (2001). *Experimental Mechanics* **41**, 19.

Rubinstein, A.A. and Xu, K. (1992). *Journal of the Mechanics and Physics of Solids* **40**, 105.

Tada, H., Paris, P.C. and Irwin, G.R. (2000). *The Stress Analysis of Cracks Handbook*, 3rd ed., The American Society of Mechanical Engineers, New York.

Thouless, M.D. (1989). *Acta Metallurgica* **37**, 2297.

Yang, C.C., Tsai, W.B., Quin, S. and Mura, T. (1991). *Composite Engineering* **1**, 113.